PAPER

Check for updates

Functional nickel iron sulphide/hydroxide catalysts for hydrazine oxidation and energy saving hydrogen production†

Pooja J. Sharma,[a] Kinjal K. Joshi,[a] Parikshit Sahatiya, [b] C. K. Sumesh [a] and Pratik M. Pataniya [*a]

Electrocatalytic water splitting is a promising technique for green hydrogen production, yet its efficiency is hindered by the sluggish oxygen evolution reaction (OER) at the anode. This study advocates an efficient strategy to address this challenge by developing a NiFe-hydroxide/sulfide heterostructure (NFS@NF) catalyst directly grown on nickel foam *via* a one-pot chemical bath deposition technique. The optimized NiFe-hydroxide/sulfide shows obvious catalytic performance, requiring overpotentials of 150 mV at a current of 10 mA cm^{-2} for hydrogen evolution. Additionally, the NFS@NF exhibits low potentials for the OER (1.45 V *vs.* RHE), urea oxidation (1.35 V *vs.* RHE), and hydrazine oxidation (0.26 V *vs.* RHE) at 100 mA cm^{-2}. These exceptional catalytic activities are attributed to the synergy between nickel and iron and sulfur-induced modifications in chemical states and the local structure. A full-cell configuration generates 10 mA cm^{-2} current at 1.57 V for water electrolysis, which can be further reduced to 1.44 V and 0.37 V by substituting conventional electrolysis of water with electrolysis of urea and hydrazine, respectively. The electrodes exhibit excellent durability, maintaining stable catalytic performance for 70 hours at 300 mA cm^{-2} for water electrolysis and 100 mA cm^{-2} for hydrazine electrolysis. Additionally, its application in an Mg/seawater battery shows stable discharge for 16 hours with a power density of 4.02 mW cm^{-2}, which provides the required power for hydrazine electrolysis. Finally, this research offers an efficient, earth-abundant catalyst solution for sustainable hydrogen production and energy storage applications, advancing hybrid water-splitting and Mg/seawater battery technologies.

Introduction

The rising worldwide energy demand and the adverse environmental effects of fossil fuel consumption have driven extensive research into sustainable and green energy sources. Molecular hydrogen (H$_2$) stands out as the most promising clean energy carrier among various alternatives due to its high energy density and the fact that its combustion produces only water as a by-product. Traditional techniques of hydrogen synthesis, such as steam methane reforming and electrolysis of water, encounter challenges including high energy consumption and carbon emissions. Particularly, the traditional water electrolysis system works through two half-reactions: cathodic hydrogen evolution and anodic oxygen evolution.[1] However, the oxygen evolution reaction (OER) exhibits a thermodynamic potential of 1.23 V *vs.* RHE (reversible hydrogen electrode), making water electrolysis more sluggish and energy consuming.[2,3]

Recent advancements have focused on developing more efficient and sustainable methods for hydrogen generation, bypassing the OER by advanced oxidation of organic compounds such as urea,[4,5] glycerol,[6,7] ethylene glycol,[8] sulphite compounds,[9] polyethylene terephthalate,[10,11] hydrazine, *etc.* One such economically viable and pollution-free approach is the simultaneous production of hydrogen coupled with hydrazine oxidation. Hydrazine (N$_2$H$_4$) has captivated attention due to the potential for complete electrocatalytic oxidation to nitrogen and water. The hydrazine oxidation reaction (HzOR) with a low thermodynamic potential of −0.33 V *vs.* RHE not only lowers the energy usage, but also facilitates the degradation of hydrazine as a pollutant in industrial and agricultural wastewater and its upgradation into value-added products.[12–14] The electrolysis system containing a hydrazine-rich electrolyte involves the HER on the cathode and HzOR on the anode. As a result of the complex intermediate adsorption/desorption processes involved in both of these activities, electrocatalysts with lower energy barriers and accelerated reaction kinetics are required.[15,16]

^{a}Department of Physical Sciences, P. D. Patel Institute of Applied Sciences, Charotar University of Science and Technology, CHARUSAT, Anand-388421, Gujarat, India. E-mail: pm.pataniya9991@gmail.com

^{b}Department of Electrical and Electronics Engineering, BITS Pilani Hyderabad, Secunderabad – 500078, India

† Electronic supplementary information (ESI) available. See DOI: https://doi.org/10.1039/d4ta08796h

This journal is © The Royal Society of Chemistry 2025

J. Mater. Chem. A, 2025, **13**, 9865–9877 | 9865

To address the technological barriers for hydrazine-assisted water electrolysis, efforts have been made to develop bi-functional electrocatalysts for the HER and HzOR. Recently, a variety of self-supported catalytic networks based on nano-arrays on Ni or Cu-foam/foil and carbon fabric have been widely explored, containing the active catalysts based on noble metals (such as Pt, Pd and Ru)[17–19] and transition metals (such as Ni, Co, Fe, Mn, *etc.*). However, the natural scarcity and high cost of noble metals make noble catalysts less attractive for industrial applications. So far, transition metal phosphides,[20,21] sulphides,[22,23] nitrides,[24] carbides,[25] hydroxides,[26] oxides,[27,28] *etc.* with optimized chemical and electronic structures have been developed. Metal/non-metal doping is a promising strategy to modify the energy levels and improve the bi-functional catalytic performance.[20] For example, Kaili Wu *et al.* reported Mn-doped 2D-NiCo-hydroxide nanosheets intertwined with 1D-carbon nanotubes with regulation of electronic structure and optimized adsorption of OH^-.[26] Wenhao Zhang *et al.* recently reported a novel 2D/3D hierarchical structure of Fe, F co-doped Ni_2P as a core with an optimised electronic structure and an armour shield of nitrogen carbon to prevent core corrosion.[20] The interface engineering strategy in a $Ni(OH)_2/Ni_2P$ heterostructure synthesized by a three-step process (electrodeposition–phosphorization–electrodeposition) shows promising bi-functional HER and HzOR catalytic performance with overpotentials of 72 mV and 14 mV to generate 10 mA cm^{-2}, respectively due to the strong synergistic effect of $Ni(OH)_2$ and Ni_2P.[21] Moreover, this process not only produces nitrogen gas and protons but also releases electrons, which can be harnessed to produce electrical energy or drive other electrochemical reactions, such as hydrogen production at the cathode.[29–33] Fu Sun *et al.* developed a hydrazine fuel cell to power the electrolyser cell for hydrazine-assisted seawater splitting.[34] They demonstrated hydrogen production at a yield of 9.2 mol h^{-1} g$_{cat}$$^{-1}$ on NiCo/MXene-based electrodes with a power consumption of 2.75 kW h per m^3 H$_2$ at a higher current density of 500 mA cm^{-2}, reporting 48% less power as compared to commercial water electrolysers.[34] Moreover, the Ni–Fe–OH amorphous layer on crystalline Ni_3S_2 supported on Ni-foam not only enhanced the catalytic OER performance in alkaline conditions, but also enhanced the corrosion resistance, ensuring the stability of electrodes at an industrial scale current density of 1000 mA cm^{-2} for 50 hours.[35] Apart from this, the optimization of electronic structure by forming heterostructures can significantly improve the electronic charge transfer,[36–39] which in turn enhances the electrochemical performance.

Inspired by this, we report the facile and one-pot synthesis of Ni_xFe_{1-x}-hydroxide/sulphide heterostructure catalysts on Ni-foam using chemical bath deposition (CBD), which is also extended up to industrial scale synthesis without using any polymeric binders. We demonstrate efficient water electrolysis and energy-saving hydrazine-assisted water electrolysis at industrial-scale current densities as well as Mg/seawater battery application. The rational design of the Ni_xFe_{1-x}-hydroxide/sulphide heterostructure electrodes and optimized chemical configuration lead to stable catalytic performance for water and

hydrazine-assisted water electrolysis at a current density of 300 mA cm^{-2}, along with low cell voltages of 1.83 V and 0.84 V, respectively. In addition, we fabricated a Mg/seawater battery with magnesium alloy (AZ31) as an anode and a Ni_xFe_{1-x}-hydroxide/sulphide heterostructure as a cathode to achieve a peak power density of up to 4.02 mW cm^{-2}. The present findings advocate the development of a state-of-the-art catalytic network for simultaneous hydrogen production and degradation of toxic hydrazine to value-added products such as nitrogen and water. This discovery holds significant promise for the effective conversion and usage of the limitless seawater resource since it offers a novel and effective method for obtaining hydrogen from seawater in real time without the need for external power networks.

Experimental section

Chemicals and reagents

Nickel nitrate hexahydrate ($Ni(NO_3)_2 \cdot 6H_2O$), iron nitrate non-ahydrate ($Fe(NO_3)_3 \cdot 9H_2O$), ammonium fluoride (NH_4F), urea (CH_4N_2O), sodium thiosulfate ($Na_2S_2O_3$), and hydrochloric acid (HCl) were purchased commercially and utilized without further purification.

Synthesis of NiFe(OH)$_2$@NF

Nickel foam-supported NiFe-hydroxide catalysts were fabricated using the chemical bath deposition technique. Prior to deposition, a (2 cm × 3 cm) piece of NF was cleaned following a routine procedure. In a typical procedure 10 mmol of ($Ni(NO_3)_2 \cdot 6H_2O$) and 10 mmol of $Fe(NO_3)_3 \cdot 9H_2O$ were dissolved in 30 ml of DI water. After 10 min of vigorously stirring, 20 mmol of NH_4F and 50 mmol of urea were added into the solution at room temperature. After completely dissolving the salts, the pre-treated NF was immersed into the reaction solution and kept at 85 °C for 5 hours. Then the electrodes were washed with DI water and dried in an oven for 5 h to obtain NiFe-hydroxide and then utilized for electrochemical experiments without additional modification.

Synthesis of the Ni$_x$Fe$_{1-x}$-hydroxide/sulphide heterostructure

To synthesise the Ni_xFe_{1-x}-hydroxide/sulphide heterostructure, Ni $(NO_3)_2 \cdot 6H_2O$ and Fe $(NO_3)_3 \cdot 9H_2O$ (with a fixed total of 20 mmol of metal but different Ni/Fe molar ratios) were added to 30 ml of DI water in appropriate proportions. After vigorous stirring for 10 minutes, 60 mmol of sodium thiosulfate ($Na_2S_2O_3$), 20 mmol of NH_4F and 50 mmol of urea were added and stirred for 30 min to obtain a homogeneous solution. Pre-treated NF was immersed in a reaction solution and maintained at 85 °C for 5 hours. In the precursor composition, the Ni/Fe molar ratio was changed to $Ni_{0.25}Fe_{0.75}$, $Ni_{0.50}Fe_{0.50}$, and $Ni_{0.75}Fe_{0.25}$, denoted as NFS-1@NF, NFS-2@NF, and NFS-3@NF respectively. NiS@NF and FeS@NF reference electrodes were also synthesized using the same procedure given above except for the absence of Fe $(NO_3)_3 \cdot 9H_2O$ and Ni $(NO_3)_2 \cdot 6H_2O$ respectively.

9866 | *J. Mater. Chem. A*, 2025, **13**, 9865–9877

This journal is © The Royal Society of Chemistry 2025

Structural characterization

The microstructure, morphology, and elemental mapping of the prepared samples were characterized using a Field Emission Scanning electron microscope with an EDAX facility (using an FEI LoVac Apreo electron microscope) and transmission electron microscopy (TEM, JEOL JAM 2100 microscope operated at 200 KeV). X-ray diffraction (XRD, make: Bruker, D2-Phasor, Cu(Kα)) was used to examine the crystal structure of the prepared samples with 2θ ranging from 10 to 70°. The chemical valence states of the corresponding elements were detected using X-ray photoelectron spectroscopy (XPS) measurements on a Thermo Scientific K-alpha XPS.

Electrochemical measurements

Electrochemical measurements were performed using a three-electrode setup with a platinum rod as the counter electrode, Ag/AgCl as a reference electrode, and the prepared electrode of area 1 cm^2 as a working electrode on an electrochemical workstation (METROHM AUTOLAB PGSTAT M204). All the measurements were carried out at room temperature. All potentials were recorded *versus* RHE using the Nernst equation: E (*vs.* RHE) $= E_{Ag/AgCl} + 0.1976 + (0.059 \times pH)$. Linear polarization curves were recorded at a scan rate of 2 mV s^{-1}. Electrochemical impedance spectroscopy (EIS) was carried out at a frequency range of 0.01 Hz to 100 kHz with an amplitude of

10 mV. The electrochemically active surface area (ECSA) was calculated from the C_{dl} using the equation ECSA $= C_{dl}/C_s$, where C_s is assumed to be 0.040 mF cm^{-2} in alkaline conditions.

Results and discussion

The structural properties of the as-prepared electrodes were investigated using the X-ray diffraction technique. Fig. 1a displays the XRD pattern of the as-prepared electrocatalysts. The diffraction peaks observed at angles of 43.8° and 51.2° in every sample correspond to the NF substrate, which is well matched with the standard data (JCPDS No. 04-0850). The formation of the Ni$_x$Fe$_{1-x}$-hydroxide/sulphide heterostructure is confirmed from the other diffraction patterns, which are well indexed to the standard XRD patterns of NiFe LDH (JCPDS No. 40-0215),[40] NiS (JCPDS No. 12-0041),[41,42] and FeS (JCPDS No. 15-0037)[43,44] displayed by symbols "∇", "θ", and "*" respectively. Fig. 1b–g display the FE-SEM images of the Ni$_x$Fe$_{1-x}$-hydroxide/ sulphide heterostructure. Fig. 1b shows the morphology of NiS@NF that covers the NF uniformly and shows the floccus structure demonstrating poor crystallinity, which is consistent with the XRD data. The FESEM image of the as-synthesized FeS@NF electrode demonstrates a nanowire-like morphology (Fig. 1c). The FeS@NF nanowires have a length of ∼0.5 µm and a diameter of ∼70 nm. The morphology of NiFe LDH shows
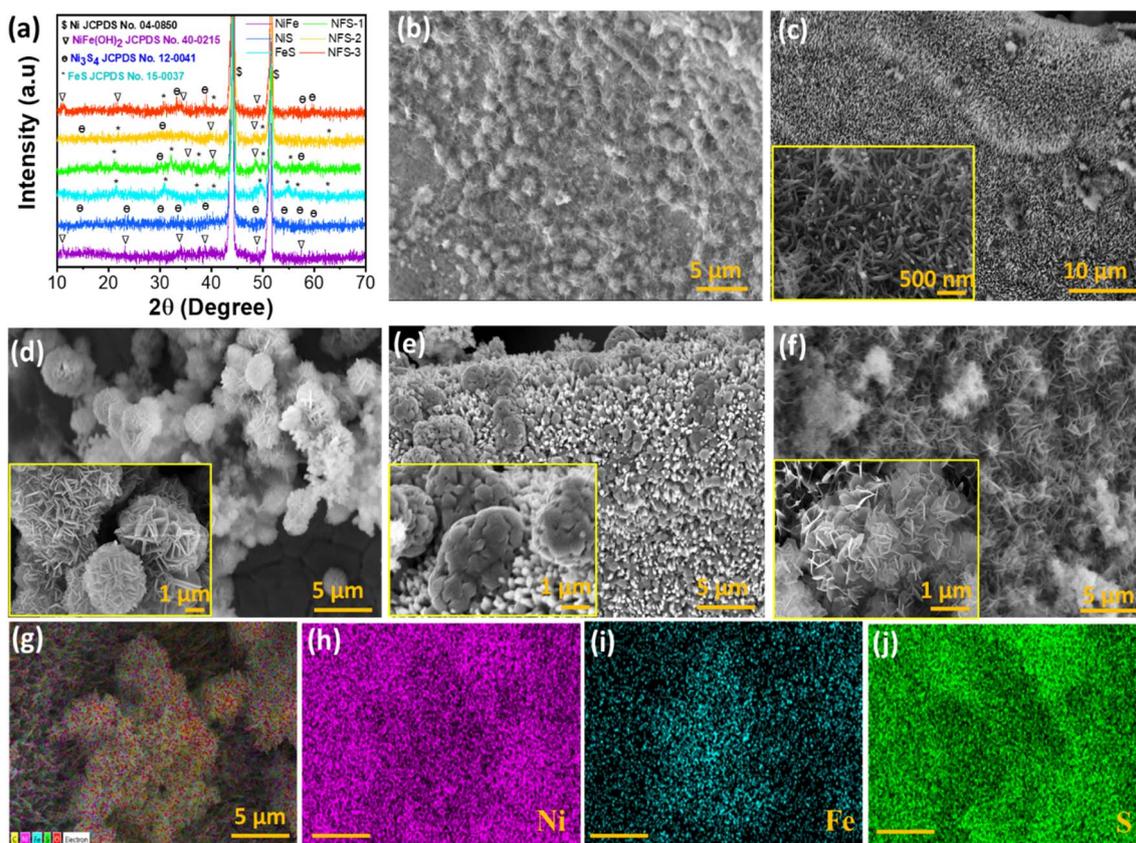

Fig. 1 (a) XRD pattern of the Ni$_x$Fe$_{1-x}$-hydroxide/sulphide heterostructure, (b–g) FE-SEM images of (b) NiS@NF, (c) FeS@NF, (d) NiFe(OH)$_2$@NF, (e) NFS-1@NF, and (f) NFS-2@NF, and (g–j) EDS elemental mapping images of NFS-2@NF catalysts.

This journal is © The Royal Society of Chemistry 2025

J. Mater. Chem. A, 2025, **13**, 9865–9877 | **9867**

enormous nanoflowers made up of nanosheets with cluster sizes of 3–4 μm (Fig. 1d). After incorporation of the sulphur source and increasing the iron content (Ni : Fe = 1 : 3, NFS-1@NF), the cross-linked clusters of nanowires and nanosheets are seen, wherein the nanosheets agglomerate and are formed on the nanowire array (Fig. 1e). With the equal ratio of Ni : Fe the NFS-2@NF electrode shows a microporous nanostructured morphology with interconnecting vertically aligned nanosheets (Fig. 1f). During water electrolysis, the nanosheet array structure can offer a large number of reaction sites to speed up the electrolyte permeation and bubble release.[45] When the Ni content increases (Ni : Fe = 3 : 1), the nanosheets no longer assemble and disperse on the underlying nanowire array as shown in Fig. S1a (ESI).† Overall the Ni_xFe_{1-x}-hydroxide/sulphide heterostructure shows nanostructure morphology such as nanosheets (NSs) and nanowires (NWs) which is advantageous for overall water splitting.[46,47] This is because through morphological design and engineering, important characteristics like specific surface area and electrical conductivity can be controlled.[45] Morphology engineering of electrocatalysts can improve the electrochemical process by offering a shorter charge transport path and better charge separation, which will support the HER and OER.[48] The energy dispersive

spectroscopic (EDS) mapping results of the NFS-2@NF electrode (Fig. 1g–j) show that the hierarchical nanostructures of elements Ni, Fe, and S are uniformly distributed in the as-formed nanosheets. Further, the TEM images of NFS-2 catalysts show a nanosheet-like morphology along with the presence of defects (Fig. S2, ESI†). The optimized defect concentration may enhance the catalytic performance for electrolysis.[49–51] TEM-EDS elemental mapping images show the presence of Ni, Fe, S and O elements on nanosheets of the NFS-2 catalyst (Fig. S3, ESI†).

The XPS spectra of the Ni_xFe_{1-x}-hydroxide/sulphide are displayed in Fig. 2. Ni, Fe, and S, the three primary constituent elements, were verified to be present in the electrode (Fig. S1b, ESI†). The high-resolution Ni 2p spectrum of Ni_xFe_{1-x}-hydroxide/sulphide in Fig. 2a shows two characteristic peaks located at 855.15 and 872.51 eV. These peaks are assigned to Ni $2p_{3/2}$ and Ni $2p_{1/2}$, respectively. The other two peaks at the binding energies of 861.05 and 878.87 eV are the satellite peaks. Compared to NiFe(OH)$_2$@NF and NiS@NF, the binding energy of Ni $2p_{3/2}$ and Ni $2p_{1/2}$ in NFS-2@NF is negatively shifted, indicating the enhanced electronic charge density around Ni sites. Previous theoretical studies also suggest that the Fe sites facilitate the transfer of electrons from Fe to Ni sites, which is
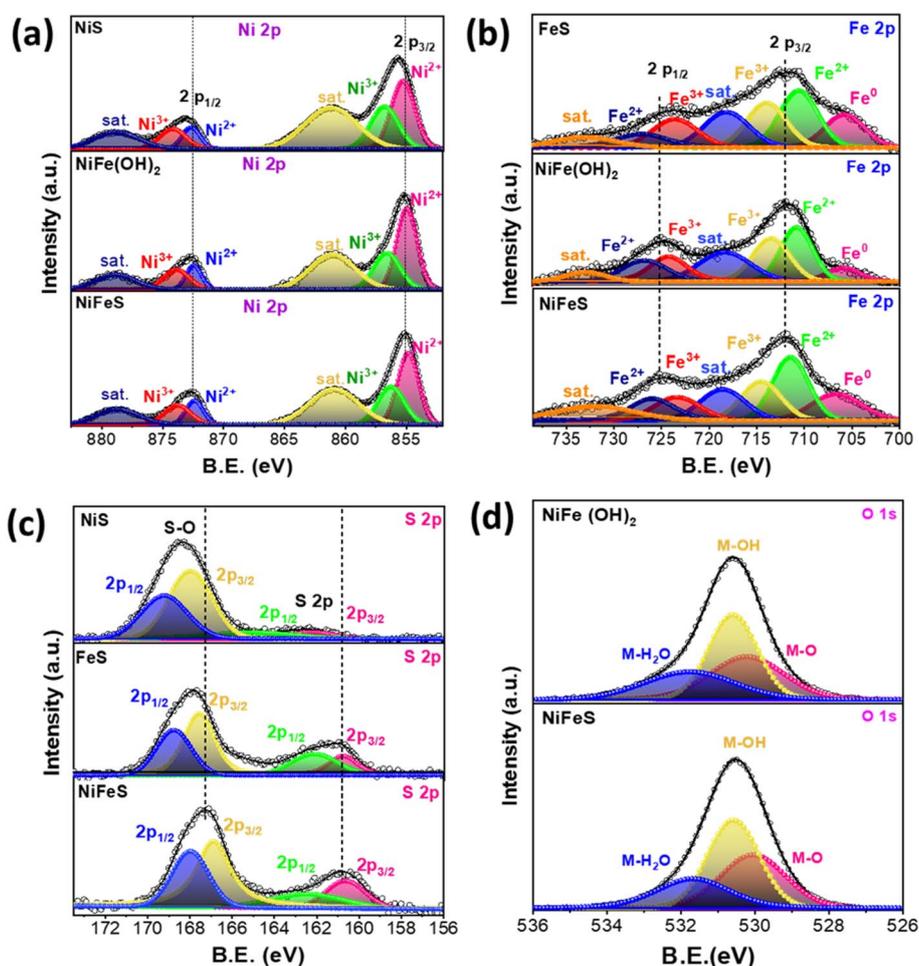

Fig. 2 XPS spectra of the Ni_xFe_{1-x}-hydroxide/sulphide heterostructure: (a) Ni 2p, (b) Fe 2p, (c) S 2p, and (d) O 1s.

9868 | *J. Mater. Chem. A*, 2025, **13**, 9865–9877

This journal is © The Royal Society of Chemistry 2025

beneficial for the enhanced conductivity of NiFe catalysts.[52–55] Additionally, the presence of Sulfur anions induces negative shifting of Ni 2p peaks in NFS-2@NF because it can be easily polarized to share more electrons with nearby metal ions, in order to balance the strong positive fields of Ni. Moreover, the incorporation of sulfur increased the catalytic activity by reducing the free energy gap between O* and OH* and the free energy of OH* adsorption.[56] Consequently, it enhances the catalytic activity for water splitting and facilitates the simultaneous processes of adsorption, electron transfer, and desorption.[56–59] Fig. 2b shows the high-resolution Fe 2p spectra of the Ni_xFe_{1-x}-hydroxide/sulphide heterostructure. The peaks associated with the binding energies of 711.97 and 725.16 eV correspond to Fe $2p_{3/2}$ and Fe $2p_{1/2}$ core levels respectively. Furthermore, compared to NiFe(OH)$_2$@NF and FeS@NF, the peak position of Fe $2p_{3/2}$ for NFS-2@NF showed a 0.37 and 0.62 eV positive shift, confirming the charge transfer from Fe to Ni due to the synergistic effect.[52–55] This finding indicates that charge transfer and electron rearrangement are induced between the components at the heterogeneous interface between metal sulfides and hydroxide, which could increase the catalytic activity of materials. The S 2p XPS spectrum of the Ni_xFe_{1-x}-hydroxide/sulphide heterostructure shows the two prominent peaks located at 167.28 and 160.75 eV assigned to sulfate groups (S–O) and S 2p respectively, indicating that sulfur was incorporated into NiFe(OH)$_2$ (ref. 59 and 60) (Fig. 2c). Fig. 2d displays the high-resolution O 1s spectra of NiFe(OH)$_2$@NF and NFS-2@NF catalysts. The peaks located at 530, 530.59, and 531.76 eV are ascribed to metal–O (M–O),

hydroxyl oxygen attached to metal (M–OH), and absorbed molecular water (M–H$_2$O), respectively.[61,62]

Hydrogen evolution reaction

We first investigate the electrocatalytic HER activity of the NiFe(OH)$_2$, NiS@NF, FeS@NF, NFS-1@NF, NFS-2@NF and NFS-3@NF catalysts in 1.0 M KOH solution using a three-electrode setup. For comparison nickel foam and Pt/C were also investigated under the same conditions. Fig. 3a illustrates the *iR*-compensated HER polarization curves of all samples. Except the bare NF, all electrocatalysts exhibit obvious catalytic HER performance. The overpotential required for NiFe(OH)$_2$, NiS@NF, FeS@NF, NFS-1@NF, NFS-2@NF and NFS-3@NF catalysts to reach 10 and 400 mA cm^{-2} current density is (204 mV, 396 mV), (192 mV, 334 mV), (158 mV, 348 mV), (180 mV, 311 mV), (150 mV, 273 mV) and (165 mV, 398 mV) respectively, whereas the commercial Pt/C required 43 mV at 10 mA cm^{-2} current density. Encouragingly, NFS-2@NF requires the minimum overpotential owing to enhanced HER performance. Tafel slopes were also calculated from the polarization curves to further comprehend the reaction kinetics of the HER (Fig. 3b). NFS-2@NF showed a lower Tafel slope (91 mV dec^{-1}) compared to NiFe (125 mV dec^{-1}), NiS (105 mV dec^{-1}), FeS (126 mV dec^{-1}), NFS-1 (95 mV dec^{-1}), and NFS-3 (124 mV dec^{-1}) indicating favourable kinetics for efficient charge and mass transport characteristics. The Tafel study indicates that the HER process occurs *via* the Volmer–Heyrovsky reaction mechanism and electrochemical desorption is the rate-determining
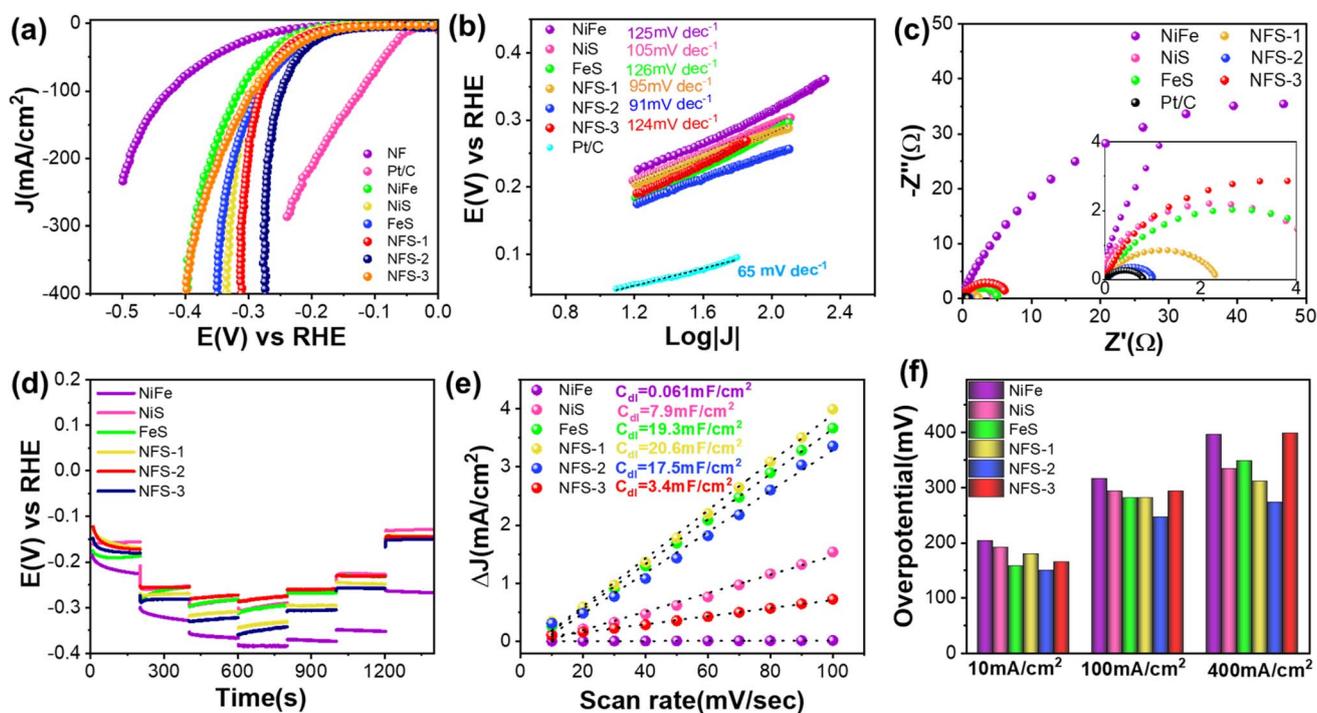

Fig. 3 HER performance of Ni_xFe_{1-x}-hydroxide/sulphide in 1.0 M KOH: (a) LSV polarization curves of Ni_xFe_{1-x}-hydroxide/sulphide, NF and Pt/C. (b) Tafel plots, (c) EIS graph, (d) accelerated chrono at 10, 100, 200 and 300 mA cm^{-2}, (e) C_{dl} graph, (f) overpotential table at 10, 100 and 400 mA cm^{-2}.

This journal is © The Royal Society of Chemistry 2025

J. Mater. Chem. A, 2025, **13**, 9865–9877 | **9869**

step.[4,63,64] Further, EIS spectra were analysed to study the charge transport on the electrode and interfacial resistance. The EIS spectra (Fig. 3c) show that NFS-2@NF exhibits the lowest charge transfer resistance value (0.98 Ω), owing to the higher conductivity and accelerated charge transport. The variation of R_{ct} for studied electrodes is consistent with the polarization and Tafel plots. In addition, the Ni_xFe_{1-x}-hydroxide/sulphide was tested for durability at various current values using the multi-step chrono-potentiometry test, as shown in Fig. 3d. Increasing the current density from 10 to 300 mA cm^{-2} resulted in higher overpotential values, which remained stable at all current density levels. Furthermore, when the current density is reduced to 10 mA cm^{-2}, the electrocatalyst's retention capability improves significantly. The steep change in the potential on switching the current is attributed to the stable charge and mass transport on electrodes.[5] The electrochemical active surface area (ECSA) was measured using cyclic voltammetry (CV) to determine the number of reactive sites. CV curves of the prepared samples were recorded at scan rates ranging from 10 to 100 mV s^{-1} in the non-faradaic potential region, as shown in Fig. S4 (ESI).† The double-layer capacitance (C_{dl}) was also estimated by fitting linearly dependent plots of current density and scan rates (Fig. 3e). Fig. 3f shows a comparison of the overpotential of Ni_xFe_{1-x}-hydroxide/sulphide at 10, 100 and 400 mA cm^{-2} current density. It is observed that at a lower overpotential, NFS-2@NF has higher catalytic activity. The NFS-2@NF also demonstrates superior HER catalytic activity compared to other transition metal-based electrocatalysts (Table S1†).

Oxygen evolution reaction

The NiFe-hydroxide/sulphide heterostructure with different combinations of Ni and Fe displayed varying electrocatalytic activities for the OER. Fig. 4a shows the polarization curves of NiFe(OH)$_2$, NiS@NF, FeS@NF, NFS-1@NF, NFS-2@NF, NFS-3@NF, bare NF and commercial RuO$_2$@NF in 1 M KOH. The polarization curves display a typical oxidation peak around 1.3 to 1.4 V, indicating the characteristic oxidation of Ni(II) to Ni(III) due to the in situ formation of NiOOH species on the surface of electrodes.[4,63] Among all fabricated electrodes, the NFS-2@NF requires the lowest potentials of 1.34 and 1.51 V (vs. RHE) to yield 10 and 400 mA cm^{-2} current density, showing superior OER performance as compared to NiFe(OH)$_2$@NF (1.45 V, 1.57 V), NiS@NF (1.49 V, 1.63 V), FeS@NF (1.35 V, 1.54 V), NFS-1@NF (1.34 V, 1.59 V), and NFS-3@NF (1.34 V, 1.56 V) catalysts. The NFS-2@NF also demonstrates superior OER catalytic activity compared to previously reported state-of-the art transition metal-based electrocatalysts (Table S2†).

Although an anodic oxygen evolution reaction (OER) is ecologically favourable, its large overpotential reduces the efficiency and cost of electrocatalytic cells. Hybrid water electrolysis using easily oxidizable chemicals like urea and hydrazine is a more efficient approach that requires a lower voltage. Urea, a major metabolic waste, has better oxidation kinetics than water. To reduce the energy consumption and remediation of the environment, we examined the urea oxidation reaction of

Ni_xFe_{1-x}-hydroxide/sulphide electrodes in a 1.0 M KOH electrolyte containing 0.33 M urea. Fig. 4d illustrates the LSV polarization curve of the Ni_xFe_{1-x}-hydroxide/sulphide heterostructure. The NFS-2@NF catalyst demonstrates superior performance compared to other prepared catalysts. Concretely, the NFS-2@NF electrode requires just 1.32 V and 1.35 V (vs. RHE) to achieve 10 and 100 mA cm^{-2} urea oxidation current density which is very low compared to other prepared catalysts such as NiFe(OH)$_2$@NF (1.36 V, 1.43 V (vs. RHE)), NiS@NF (1.32 V, 1.36 V (vs. RHE)), FeS@NF (1.33 V, 1.37 V (vs. RHE)), NFS-1@NF (1.334 V, 1.38 V (vs. RHE)), and NFS-3@NF (1.328 V, 1.37 V (vs. RHE)). The NFS-2@NF exhibits exceptional properties of dissolving urea molecules, significantly better than previously reported materials (Table S3†).

Moreover, hydrazine is also a type of water contaminant and liquid rocket fuel; its theoretical oxidation potential (−0.33 V) is much lower than that of water (1.23 V) and urea (0.37 V), making it a potential energy-saving alternative to the OER. In addition, the HzOR generates environmentally supportive products such as nitrogen and water, making it a more energy-efficient approach. Fig. 4g shows the electrocatalytic activity of the as-prepared catalysts in 1.0 M KOH + 0.3 M hydrazine hydrate (HH) electrolyte. As with the OER and UOR, the catalytic activity of the HzOR over the NiFe(OH)$_2$ is substantially inferior to that of the other prepared electrodes. The NiFe(OH)$_2$@NF, NiS@NF, FeS@NF, NFS-1@NF, and NFS-3@NF required 0.89 V (vs. RHE), 0.79 V (vs. RHE), 0.19 V (vs. RHE), 0.30 V (vs. RHE), and 0.20 V (vs. RHE) potentials to reach 10 mA cm^{-2} current density. The NFS-2@NF which demonstrates exceptional performance towards the HzOR needs only 0.18 and 0.25 V (vs. RHE) to reach 10 and 100 mA cm^{-2} current density suggesting its capabilities as a highly active catalyst for the HzOR process. Moreover, OER, UOR, and HzOR electrochemical impedance spectroscopy (EIS) was conducted to analyze ion transport during electrocatalysis reactions. As shown in Fig. 4b, e and h NFS-2@NF formed the shortest semicircle, while the NiFe-hydroxide produced the largest. The small semi-circle radius leads to lower charge-transfer resistance, improved electrical conductivity, and faster reaction kinetics. It demonstrates that optimized concentrations of Ni and Fe modulate the atomic arrangement and optimize the electronic structure resulting in improved conductivity. Furthermore, Tafel slopes were analysed from linear sweep voltammetry (LSV) curves of the Ni_xFe_{1-x}-hydroxide/sulphide heterostructure to further study reaction kinetics. As shown in Fig. 4c, f and i the Tafel slope of NiFe(OH)$_2$, NiS@NF, FeS@NF, NFS-1@NF, NFS-2@NF and NFS-3@NF demonstrates that the NFS-2@NF electrode is more effective in enhancing the reaction kinetics of anodic oxygen. The NFS-2@NF shows the lowest OER, UOR, and HzOR Tafel slopes due to the improved mass transfer rate and electron transfer pathways at the interface. Excellent activity could be attributed to the synergistic effect of structure and composition. The Ni_xFe_{1-x}-hydroxide/sulphide heterostructure is a multifunctional electrocatalyst for anodic oxidation processes, as demonstrated by the above results. This Ni_xFe_{1-x}-hydroxide/sulphide heterostructure array supports the concept of
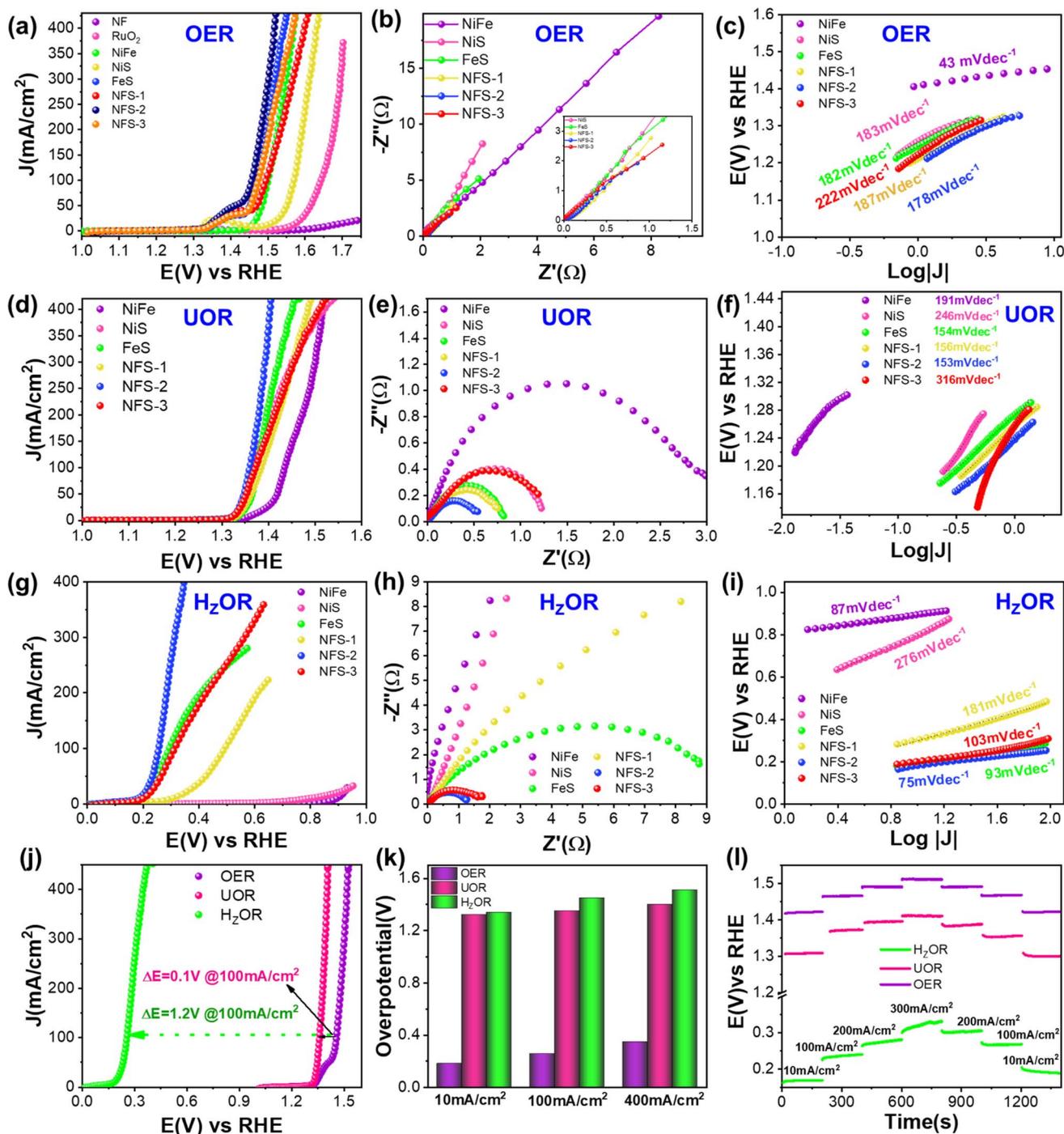
9870 | J. Mater. Chem. A, 2025, **13**, 9865–9877

This journal is © The Royal Society of Chemistry 2025

Fig. 4 OER, UOR, and HzOR performance of Ni$_x$Fe$_{1-x}$-hydroxide/sulphide catalysts: (a) OER polarization curves of Ni$_x$Fe$_{1-x}$S@NF, NF and RuO$_2$, (b) EIS graph, (c) Tafel plots, (d) UOR polarization curves of Ni$_x$Fe$_{1-x}$S@NF, (e) EIS graph, (f) Tafel plots, (g) HzOR polarization curves of Ni$_x$Fe$_{1-x}$-hydroxide/sulphide, (h) EIS graph, (i) Tafel plots, (j) comparison of LSV curves in various media, (k) overpotential table at 10, 100 and 400 mA cm^{-2}, (l) accelerated chrono at 10, 100, 200 and 300 mA cm^{-2}.

replacing the slow OER with the UOR or HzOR, leading to new energy-saving and wastewater treatment possibilities.

Fig. 4j displays the LSV curves of NFS-2@NF for the OER, UOR and HzOR. As observed, the performance of the NFS-2@NF catalyst was improved by adding 0.33 M urea in 1.0 M KOH solution; however, in 1.0 M KOH with 0.3 M HH, it showed

superior catalytic activity owing to low thermodynamic potential of oxidation of hydrazine. Fig. 4k shows that the voltages for HzOR to obtain current densities of 10, 50, and 100 mA cm^{-2} are 0.18 V, 0.23 V, and 0.25 V, which are significantly lower than those for the UOR (1.32 V, 1.34 V, and 1.35 V) and OER (1.34 V, 1.41 V and 1.45 V respectively). To assess the electrochemical

This journal is © The Royal Society of Chemistry 2025

J. Mater. Chem. A, 2025, **13**, 9865–9877 | **9871**

stability of NFS-2@NF in the OER, UOR, and HzOR, a chrono-potentiometry test was carried out at 10, 100, 200, and 300 mA cm^{-2} current density as shown in Fig. 4l. The operational stability was enhanced by the ability to shift instantly at various current rates and maintain stability throughout all current density ranges. The outstanding activity is due to (i) the presence of more exposed active sites at the surface due to the nano-structured growth in the 3D NF substrate which will avoid the bubble shielding effect, and (ii) direct growth of bimetallic sulfides on the current collector NF, which enables efficient mass transfer and superior mechanical adhesion.[45,63] Additionally, the intrinsic activity of the catalysts plays a crucial role in HER and OER performance. Therefore, polarization curves normalized by double layer capacitance were calculated for NiS, FeS and NFS-2 catalysts (Fig. S5, ESI†), showing that NFS-2

exhibits higher normalized current as compared to pristine NiS and FeS due to synergy between Ni and Fe. Even previous reports on the DFT calculations demonstrated that the Fe sites serve as active catalytic sites due to stronger adsorption of the intermediates, while incorporation of S in NiFeOOH enhances the charge transfer between adsorbates and active sites, which leads to the superior catalytic performance.[65]

Water, urea, and hydrazine electrolysis full cell

We studied hydrogen production through electrolysis of water, urea and hydrazine in a two-electrode electrolyser using Ni$_x$-Fe$_{1-x}$-hydroxide/sulphide as both the anode and cathode to further understand its practical applicability in 1 M KOH, 1 M KOH + 0.33 M urea, and 1 M KOH + 0.3 M HH electrolytes.
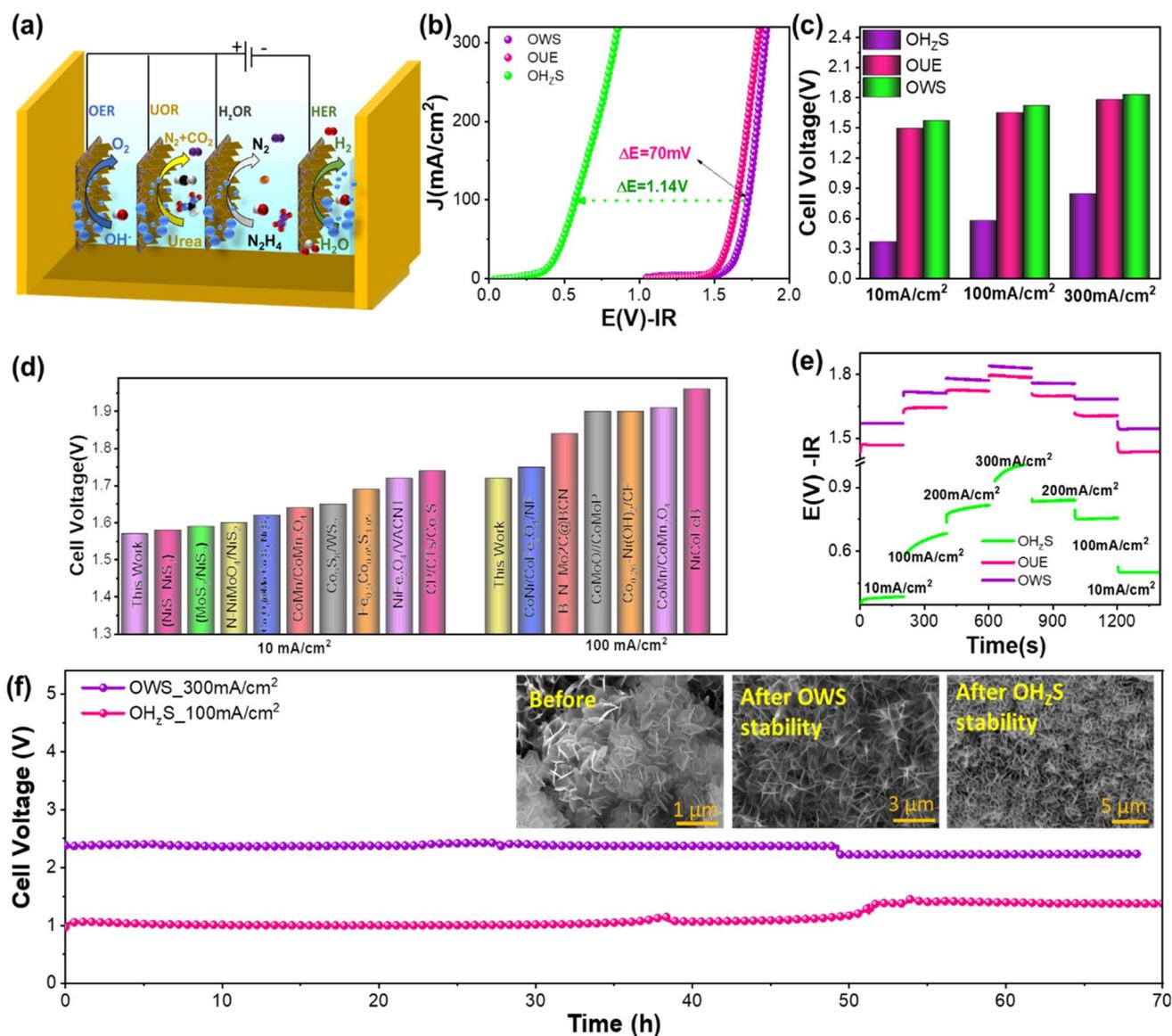

Fig. 5 (a) Schematic of overall water splitting performance, (b) LSV curve of the NFS-2@NF catalysts in 1.0 M KOH, 1.0 M KOH + 0.33 M HH, and 1.0 M KOH + 0.33 M urea electrolyte, (c) corresponding overpotential at 10, 100 and 300 mA cm^{-2} current density, (d) comparison of NFS-2@NF catalysts with recently reported work in 1.0 M KOH solution, (e) step chrono-potentiometry curve, (f) stability test for the NFS-2@NF electrode in 1.0 M KOH and 1.0 M KOH + 0.33 M HH solution.

9872 | J. Mater. Chem. A, 2025, 13, 9865–9877

This journal is © The Royal Society of Chemistry 2025

Fig. 5a presents the schematic diagram of overall water, urea, and hydrazine splitting. The linear polarization curves for overall water electrolysis (OWE), overall urea electrolysis (OUE), and overall hydrazine electrolysis (OHzE) on NFS-2@NF catalysts are shown in Fig. 5b. The negatively shifted polarization curves on potential values for OHzE demonstrate that OHzE is the energy-saving approach for green H_2 production. The comparison of cell voltage at 10, 100, and 300 mA cm^{-2} current density is shown in Fig. 5c. The cell voltages required to achieve 10, 100, and 300 mA cm^{-2} current densities for OHzE are 0.37, 0.58, and 0.84 V, which are much smaller in comparison to those of OUE (1.49, 1.65, and 1.78 V) and OWE (1.57, 1.72, and 1.83 V). Furthermore, the as-synthesized catalysts NFS-2@NF exhibit superior performance in comparison to the as-prepared catalysts NiFe(OH)$_2$@NF, NiS@NF, FeS@NF, NFS-1@NF, and NFS-3@NF (Fig. S6–8, ESI†). In addition, it also shows good activity compared to recently published reports in 1.0 M KOH solution (Fig. 5d). The chrono-potentiometry was carried out for 10 to 300 mA cm^{-2} current density as shown in Fig. 5e. With the sharp increase in cell voltage, the current density responded quickly and remained stable for the next 200 s, demonstrating the superior dimensional stability, good electrical conductivity, and quick mass and charge transportation ability of the NFS-2@NF electrode during the OWS, OUE, and OHzS reaction. As illustrated in Fig. 5f, the NFS-2@NF catalyst exhibits excellent stability at higher current densities of 300 and 100 mA cm^{-2} for time intervals over 70 h in 1.0 M KOH and 1.0 M KOH + 0.3 M HH solution, owing to the robustness of

electrodes for water and hydrazine electrolysis and capability for industrial-scale and sustainable hydrogen production. However, a slight rise in the cell voltage is found for water and hydrazine hydrolysis after continuous electrolysis for 50 hours. Furthermore, the morphology and structure of the NFS-2@NF catalyst were analysed after the stability test for water and hydrazine electrolysis. The morphology remains almost unchanged after the stability test, showing the dimensional stability of the electrode (inset of Fig. 5f). The powder XRD (Fig. S9, ESI†) pattern shows that the crystal structure of the NFS-2@NF catalyst is preserved even after long-term electrolysis, proving the robustness of the catalysts and suggesting suitability for technical application for sustainable energy production. The surface chemical composition of the NFS-2 was also analysed by XPS (Fig. S10, ESI†), showing the almost unaltered electronic structure around Ni and Fe due to the exceptional robustness of the catalyst. Additionally, NFS-2 preserves the nanosheet-like morphology after the stability test (Fig. S11, ESI†).

Mg-seawater battery performance with the Ni$_x$Fe$_{1-x}$S@NF cathode

We further investigated the practical applicability of the Ni$_x$Fe$_{1-x}$-hydroxide/sulphide heterostructure for the cathode of Mg/seawater batteries. When Mg/seawater batteries operate in hydrogen evolution mode, then they generated hydrogen at the cathode as well as producing electricity, making them a perfect power source for marine equipment. To execute this, we
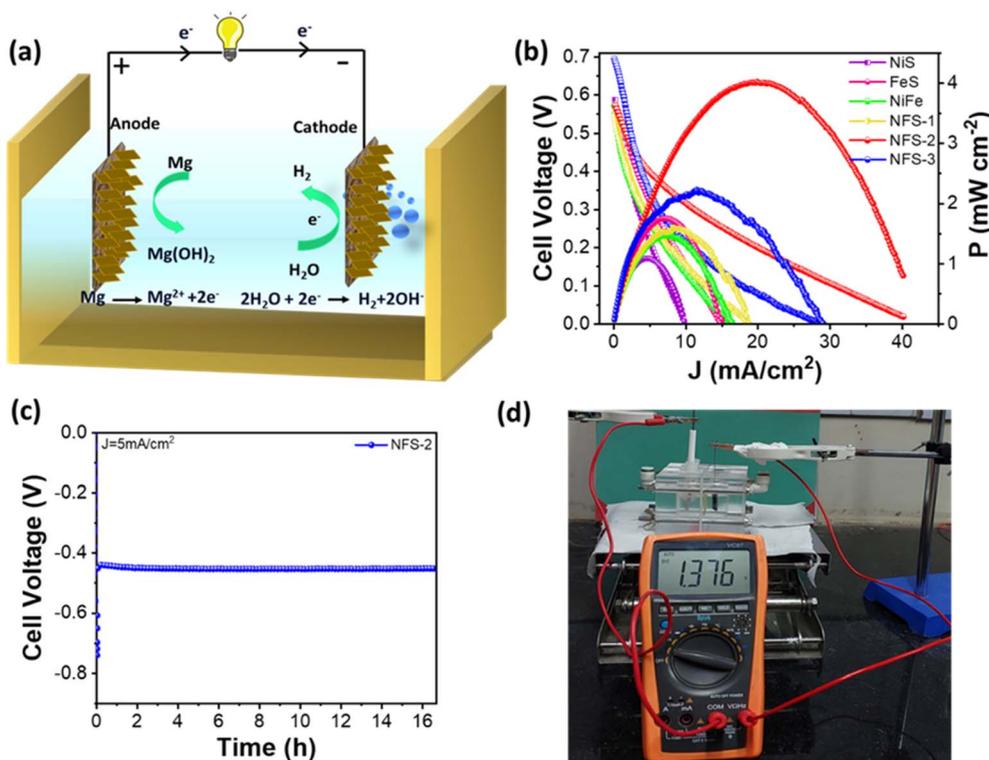

Fig. 6 (a) The structure and working principle of the Mg/seawater battery, (b) discharging curve and corresponding power density curve of the Mg/seawater battery with different cathodes, (c) stability test of the Mg/seawater battery with an NFS-2 cathode at 5 mA cm^{-2} current density, (d) open circuit voltage of the as-fabricated Mg/seawater battery pack with NFS-2 heterostructure cathodes.

constructed an Mg/seawater battery using simulated seawater (0.5 M NaCl) as the electrolyte, Ni_xFe_{1-x}-hydroxide/sulphide as the cathode, and magnesium alloy (AZ31) as the anode (Fig. 6a). Fig. 6b shows the discharging curves and corresponding power density curves of the as-assembled Mg/seawater battery. It has been observed that the open circuit voltages of Mg/seawater batteries with various cathodes reach 0.54–0.7 V. The open circuit voltage of the NFS-2@NF catalysts is highest among all the prepared catalysts. In addition, the as-assembled magnesium/seawater battery with NFS-2@NF as a cathode demonstrates a maximum output power density of up to 4.02 mW cm^{-2} at the current density of 20 mA cm^{-2}. Furthermore, stability tests were also measured under galvanostatic discharge of 5 mA cm^{-2}. As shown in Fig. 6c, the performance of the Mg/Seawater battery is almost entirely stable over 16 hours of discharging at 5 mA cm^{-2} current density demonstrating that the Mg/seawater battery with the NFS-2@NF cathode can operate for a prolonged period of time. In order to demonstrate the applicability for practical application, four Mg/seawater batteries using NFS-2@NF heterostructure cathodes and AZ31 anodes were linked in series to form a Mg/seawater battery pack. The as-assembled Mg/seawater battery pack with an operating voltage of about 1.37 V is displayed in Fig. 6d. Furthermore, the light-emitting diode (LED) display screen can be powered by the assembled Mg/seawater battery pack, as shown in Fig. S7a,† indicating potential practical applications.

Conclusions

In summary, the present research demonstrates the one-step synthesis and multifunctional applications of the Ni_xFe_{1-x}-hydroxide/sulfide (NFS) heterostructure. Self-supported NFS catalysts exhibit excellent catalytic activity for the hydrogen evolution reaction (HER), oxygen evolution reaction (OER), urea oxidation reaction (UOR), and hydrazine oxidation reaction (HzOR). Specifically, the NFS-2@NF electrode achieved overpotentials of 150 mV at 10 mA cm^{-2}, and required just 1.45 V, 1.35 V, and 0.256 V (vs. RHE) for the OER, UOR, and HzOR at 100 mA cm^{-2}, respectively. The improved catalytic activity is attributed to sulfur incorporation, the optimized Ni/Fe ratio, and the optimized nanostructured morphology, which optimize the intrinsic activity, facilitate gas product diffusion, and enhance mass transfer. Besides, the NFS electrocatalyst demonstrated exceptional potential in Mg/seawater batteries, delivering exceptional discharge stability and a peak power density of 4.02 mW cm^{-2}. Present research advocates the versatility and practicality of the NiFe hydroxide/sulfide heterostructure in addressing energy and environmental challenges.

Data availability

Data will be made available on request.

Author contributions

Pooja J. Sharma: conceptualization, methodology, investigation, visualization, data curation, writing – original draft,

writing – review & editing. Kinjal K Joshi: investigation, visualization, data curation. Parikshit Sahatiya: investigation, visualization, data curation. C. K. Sumesh: investigation, visualization, data curation. Pratik M. Pataniya: conceptualization, project administration, validation, data curation, resources, writing – review & editing.

Conflicts of interest

The authors declare that they have no known competing financial interests or personal relationships that could have appeared to influence the work reported in this paper.

Acknowledgements

References

1 P. Sanwal, A. Raza, Y.-X. Miao, B. Lumbers and G. Li, Advances in coinage metal nanoclusters: From synthesis strategies to electrocatalytic performance, *Polyoxometalates*, 2024, **3**, 9140057, DOI: **10.26599/POM.2024.9140057**.

2 W. Li, H. Tian, L. Ma, Y. Wang, X. Liu and X. Gao, Low-temperature water electrolysis: fundamentals, progress, and new strategies, *Mater. Adv.*, 2022, **3**, 5598–5644, DOI: **10.1039/d2ma00185c**.

3 X. Xu, Z. Shao and S. P. Jiang, High-Entropy Materials for Water Electrolysis, *Energy Technol.*, 2022, **10**, 2200573, DOI: **10.1002/ente.202200573**.

4 P. J. Sharma, K. H. Modi, P. Sahatiya, C. K. Sumesh and P. M. Pataniya, Electroless deposited NiP-fabric electrodes for efficient water and urea electrolysis for hydrogen production at industrial scale, *Appl. Surf. Sci.*, 2024, **644**, 158766, DOI: **10.1016/j.apsusc.2023.158766**.

5 A. M. Shah, K. H. Modi, P. M. Pataniya, K. S. Joseph, S. Dabhi, G. R. Bhadu and C. K. Sumesh, Self-Supported Mn-Ni3Se2 Electrocatalysts for Water and Urea Electrolysis for Energy-Saving Hydrogen Production, *ACS Appl. Mater. Interfaces*, 2024, **16**, 11440–11452, DOI: **10.1021/acsami.3c16244**.

6 X. Hu, J. Lu, Y. Liu, L. Chen, X. Zhang and H. Wang, Sustainable catalytic oxidation of glycerol: a review, *Environ. Chem. Lett.*, 2023, **21**, 2825–2861, DOI: **10.1007/s10311-023-01608-z**.

7 W. Ruan, C. Yuan, F. Teng, H. Liao and A. O. Ibhadon, Boosting hydrogen production in ultrathin birnessite nanosheet arrays-based electrolytic cell by glycerol and urea oxidation reactions, *Mater. Today Chem.*, 2022, **26**, 101086, DOI: **10.1016/j.mtchem.2022.101086**.

8 J. Li, L. Li, X. Ma, X. Han, C. Xing, X. Qi, R. He, J. Arbiol, H. Pan, J. Zhao, J. Deng, Y. Zhang, Y. Yang and A. Cabot, Selective Ethylene Glycol Oxidation to Formate on Nickel Selenide with Simultaneous Evolution of Hydrogen, *Adv. Sci.*, 2023, **10**, 2300841, DOI: **10.1002/advs.202300841**.

9 L. Yi, P. Shao, H. Li, M. Zhang, X. Liu, P. Wang and Z. Wen, Hybrid acid/alkali electrolysis toward industrial-scale H 2

9874 | *J. Mater. Chem. A*, 2025, **13**, 9865–9877

This journal is © The Royal Society of Chemistry 2025

generation and sulfite oxidation conversion, *Chem. Eng. J.*, 2023, **467**, 143462, DOI: **10.1016/j.cej.2023.143462**.

10 W. Li, D. Xiao, X. Gong, X. Xu, F. Ma, Z. Wang, P. Wang, Y. Liu, Y. Dai, Z. Zheng, Y. Fan and B. Huang, Electrocatalytic upgrading of polyethylene terephthalate plastic to formic acid at an industrial-scale current density via Ni-MOF @ MnCo-OH catalyst, *Chem. Eng. J.*, 2024, **480**, 148087, DOI: **10.1016/j.cej.2023.148087**.

11 H. Kang, D. He, X. Yan, B. Dao, N. B. Williams, G. I. Elliott, D. Streater, J. Nyakuchena, J. Huang, X. Pan, X. Xiao and J. Gu, Cu Promoted the Dynamic Evolution of Ni-Based Catalysts for Polyethylene Terephthalate Plastic Upcycling, *ACS Catal.*, 2024, **14**, 5314–5325, DOI: **10.1021/acscatal.3c05509**.

12 T. Y. Burshtein, Y. Yasman, L. Muñoz-Moene, J. H. Zagal and D. Eisenberg, Hydrazine Oxidation Electrocatalysis, *ACS Catal.*, 2024, **14**, 2264–2283, DOI: **10.1021/acscatal.3c05657**.

13 L. Zhu, J. Huang, G. Meng, T. Wu, C. Chen, H. Tian, Y. Chen, F. Kong, Z. Chang, X. Cui and J. Shi, Active site recovery and N-N bond breakage during hydrazine oxidation boosting the electrochemical hydrogen production, *Nat. Commun.*, 2023, **14**, 1997, DOI: **10.1038/s41467-023-37618-2**.

14 T. Y. Burshtein, K. Tamakuwala, M. Sananis, I. Grinberg, N. R. Samala and D. Eisenberg, Understanding hydrazine oxidation electrocatalysis on undoped carbon, *Phys. Chem. Chem. Phys.*, 2022, **24**, 9897–9903, DOI: **10.1039/D2CP00213B**.

15 R. G. Kadam, T. Zhang, D. Zaoralová, M. Medveď, A. Bakandritsos, O. Tomanec, M. Petr, J. Zhu Chen, J. T. Miller, M. Otyepka, R. Zbořil, T. Asefa and M. B. Gawande, Single Co-Atoms as Electrocatalysts for Efficient Hydrazine Oxidation Reaction, *Small*, 2021, **17**, 2006477, DOI: **10.1002/smll.202006477**.

16 R. Miao and R. G. Compton, The Electro-Oxidation of Hydrazine: A Self-Inhibiting Reaction, *J. Phys. Chem. Lett.*, 2021, **12**, 1601–1605, DOI: **10.1021/acs.jpclett.1c00070**.

17 X. Liu, W. Sun, X. Hu, J. Chen and Z. Wen, Self-powered H_2 generation implemented by hydrazine oxidation assisting hybrid electrochemical cell, *Chem. Eng. J.*, 2023, **474**, 145355, DOI: **10.1016/j.cej.2023.145355**.

18 W. Zhu, A. Gandi, Q. Wu, H. Yan, M. Zhao, Z. Wang and H. Liang, Simultaneous electrocatalytic hydrogen production and hydrazine removal from acidic waste water, *Chem. Eng. Sci.*, 2022, **258**, 117769, DOI: **10.1016/j.ces.2022.117769**.

19 Z. Yu, C. Si, F. Sabaté, A. P. LaGrow, Z. Tai, V. M. Diaconescu, L. Simonelli, L. Meng, M. J. Sabater, B. Li and L. Liu, Defective Ru-doped α-MnO_2 nanorods enabling efficient hydrazine oxidation for energy-saving hydrogen production via proton exchange membranes at near-neutral pH, *Chem. Eng. J.*, 2023, **470**, 144050, DOI: **10.1016/j.cej.2023.144050**.

20 W. Zhang, X. Liu, Q. Yu, X. Wang and H. Mao, In situ electronic redistribution of Ni_2P hierarchical structure for energy-saving hydrogen production in seawater, *Chem. Eng. J.*, 2023, **454**, 140210, DOI: **10.1016/j.cej.2022.140210**.

21 H. Yang, H. Wang, M. Sun and Z. Yuan, Interface engineering of bifunctional nickel hydroxide/nickel phosphide heterostructure for efficient intermittent hydrazine-assisted water splitting, *Chem. Eng. J.*, 2023, **475**, 146134, DOI: **10.1016/j.cej.2023.146134**.

22 M.-Y. Ma, H.-Z. Yu, L.-M. Deng, L.-Q. Wang, S.-Y. Liu, H. Pan, J.-W. Ren, M. Y. Maximov, F. Hu and S.-J. Peng, Interfacial engineering of heterostructured carbon-supported molybdenum cobalt sulfides for efficient overall water splitting, *Tungsten*, 2023, **5**, 589–597, DOI: **10.1007/s42864-023-00212-6**.

23 X.-Z. Ren, X.-H. Li, Y.-J. Peng, G.-Z. Wang, J. Yin, X.-C. Zhao, W. Wang and X.-B. Wang, $FeNiS_2$/reduced graphene oxide electrocatalysis with reconstruction to generate FeNi oxo/hydroxide as a highly-efficient water oxidation electrocatalyst, *Rare Met.*, 2022, **41**, 4127–4137, DOI: **10.1007/s12598-022-02104-z**.

24 Z. Li, L. Cao, T. Yang, J. He, Z. Wang, J. He, Y. Zhao and Z. Chai, Janus structural TaON/Graphene-like carbon dual-supported Pt electrocatalyst enables efficient oxygen reduction reaction, *J. Colloid Interface Sci.*, 2025, **677**, 677–686, DOI: **10.1016/j.jcis.2024.07.167**.

25 J. Wang, D. Thanh, K. Chang, S. Prabhakaran, J. Zhao, D. Hwan, N. Hoon and J. Hee, Nano Energy Hierarchical Ni @ CNTs-bridged $Mo_x C/Ni_2 P$ heterostructure micro-pillars for enhanced seawater splitting and Mg/seawater battery, *Nano Energy*, 2023, **111**, 108440, DOI: **10.1016/j.nanoen.2023.108440**.

26 K. Wu, C. Cao, K. Li, C. Lyu, J. Cheng, H. Li, P. Hu, J. Wu, W. Lau, X. Zhu, P. Qian and J. Zheng, Regulating electronic structure by Mn doping for nickel cobalt hydroxide nanosheets/carbon nanotube to promote oxygen evolution reaction and oxidation of urea and hydrazine, *Chem. Eng. J.*, 2023, **452**, 139527, DOI: **10.1016/j.cej.2022.139527**.

27 V. V Burungale, H. Bae, M. A. Gaikwad, P. Mane, J. Heo, C. Seong, S. Kang, S. Ryu and J. Ha, Cu_2O-based trifunctional catalyst for enhanced alkaline water splitting and hydrazine oxidation : Integrating sulfurization , Co incorporation , and LDH heterostructure, *Chem. Eng. J.*, 2024, **486**, 150175, DOI: **10.1016/j.cej.2024.150175**.

28 R. Arumugam, S. Jung, A. Min, C. Joo and M. Yong, Unveiling the origin of activity in $RuCoO_x$-anchored nitrogen-doped carbon electrocatalyst for high-efficiency hydrogen production and hydrazine oxidation using Raman spectroscopy, *Chem. Eng. J.*, 2023, **475**, 146441, DOI: **10.1016/j.cej.2023.146441**.

29 J. Zhang, Y. Wang, C. Yang, S. Chen, Z. Li, Y. Cheng, H. Wang, Y. Xiang, S. Lu and S. Wang, Elucidating the electro-catalytic oxidation of hydrazine over carbon nanotube-based transition metal single atom catalysts, *Nano Res.*, 2021, **14**, 4650–4657, DOI: **10.1007/s12274-021-3397-9**.

30 H. Liu, Y. Liu, M. Li, X. Liu and J. Luo, Transition-metal-based electrocatalysts for hydrazine-assisted hydrogen production, *Mater. Today Adv.*, 2020, **7**, 100083, DOI: **10.1016/j.mtadv.2020.100083**.

31 J. Park and J. Lee, Optimizing Various Operational Conditions of Hydrazine Single Cell for a Short Stack

This journal is © The Royal Society of Chemistry 2025

J. Mater. Chem. A, 2025, **13**, 9865–9877 | **9875**

System, *Adv. Energy Sustainability Res.*, 2023, **4**, 2200188, DOI: 10.1002/aesr.202200188.

32 X. Liu, H. Mao, G. Liu, Q. Yu, S. Wu and B. Li, Metal doping and Hetero-engineering of Cu-doped CoFe/Co embedded in N-doped carbon for improving trifunctional electrocatalytic activity in alkaline seawater, *Chem. Eng. J.*, 2023, **451**, 138699, DOI: 10.1016/j.cej.2022.138699.

33 J. Wang, X. Guan, H. Li, S. Zeng, R. Li, Q. Yao, H. Chen, Y. Zheng and K. Qu, Nano Energy Robust Ru-N metal-support interaction to promote self-powered H 2 production assisted by hydrazine oxidation, *Nano Energy*, 2022, **100**, 107467, DOI: 10.1016/j.nanoen.2022.107467.

34 F. Sun, J. Qin, Z. Wang, M. Yu, X. Wu, X. Sun and J. Qiu, Energy-saving hydrogen production by chlorine-free hybrid seawater splitting coupling hydrazine degradation, *Nat. Commun.*, 2021, **12**, 4182, DOI: 10.1038/s41467-021-24529-3.

35 X. Zou, Y. Liu, G.-D. Li, Y. Wu, D.-P. Liu, W. Li, H.-W. Li, D. Wang, Y. Zhang and X. Zou, Ultrafast Formation of Amorphous Bimetallic Hydroxide Films on 3D Conductive Sulfide Nanoarrays for Large-Current-Density Oxygen Evolution Electrocatalysis, *Adv. Mater.*, 2017, **29**, 1700404, DOI: 10.1002/adma.201700404.

36 X. Zhang, Z. Li, E. Hong, T. Yan and X. Fang, Effective Dual Cation Release in Quasi-2D Perovskites for Ultrafast UV Light-Powered Imaging, *Adv. Mater.*, 2025, **37**, 2412014, DOI: 10.1002/adma.202412014.

37 M. Deng, Z. Li, S. Liu, X. Fang and L. Wu, Wafer-scale integration of two-dimensional perovskite oxides towards motion recognition, *Nat. Commun.*, 2024, **15**, 8789, DOI: 10.1038/s41467-024-52840-2.

38 E. Hong, Z. Li, X. Zhang and X. Fang, Light-State Rectification Behaviors Induced by Interlayer Excitons in Mixed-Dimensional Single-Crystalline Perovskite Heterostructures, *Adv. Funct. Mater.*, 2025, **35**, 2412189, DOI: 10.1002/adfm.202412189.

39 E. Hong, Z. Li, X. Zhang, X. Fan and X. Fang, Deterministic Fabrication and Quantum-Well Modulation of Phase-Pure 2D Perovskite Heterostructures for Encrypted Light Communication, *Adv. Mater.*, 2024, **36**, 2400365, DOI: 10.1002/adma.202400365.

40 W. Liu, Z. Qin, X. Dai, S. Meng, X. Niu, W. Shi, F. Wu and X. Cao, Coupling of NiFe layered double hydroxides with sulfides for highly efficient urea electrolysis and hydrogen evolution, *Energies*, 2023, **16**, 1092.

41 Z. Ma, X. Yuan, Z. Zhang, D. Mei, L. Li, Z. F. Ma, L. Zhang, J. Yang and J. Zhang, Novel flower-like nickel sulfide as an efficient electrocatalyst for non-aqueous lithium-air batteries, *Sci. Rep.*, 2015, **5**, 1–9, DOI: 10.1038/srep18199.

42 N. A. Trivedi, M. Patel, P. M. Pataniya and C. K. Sumesh, Large area and robust NiS/Ag electrodes for hydrogen evolution reaction, *Mater. Today Proc.*, 2023, **73**, 550–552, DOI: 10.1016/j.matpr.2022.10.289.

43 J. Jin, W. Wu, H. Min, H. Wu, S. Wang, Y. Ding and S. Yang, A glassy carbon electrode modified with FeS nanosheets as a highly sensitive amperometric sensor for hydrogen peroxide, *Microchim. Acta*, 2017, **184**, 1389–1396.

44 S. Niu, W. J. Jiang, T. Tang, L. P. Yuan, H. Luo and J. S. Hu, Autogenous Growth of Hierarchical NiFe(OH)x/FeS Nanosheet-On-Microsheet Arrays for Synergistically Enhanced High-Output Water Oxidation, *Adv. Funct. Mater.*, 2019, **29**, 1–9, DOI: 10.1002/adfm.201902180.

45 P. J. Sharma, K. K. Joshi, S. Siraj, P. Sahatiya, C. K. Sumesh and P. Pataniya, Vanadium-Doped Ni3S2: Morphological Evolution for Enhanced Industrial-Scale Water and Urea Electrolysis, *ChemSusChem*, 2024, e202401371, DOI: 10.1002/cssc.202401371.

46 S. Allami, Z. D. A. Ali, Y. Li, H. Hamody, B. H. Jawad, L. Liu and T. Li, Photoelectrochemical performance of N-doped ZnO branched nanowire photoanodes, *Heliyon*, 2017, **3**, e00423, DOI: 10.1016/j.heliyon.2017.e00423.

47 A. Sreedhar, I. N. Reddy, Q. T. H. Ta, G. Namgung, E. Cho and J.-S. Noh, Facile growth of novel morphology correlated Ag/Co-doped ZnO nanowire/flake-like composites for superior photoelectrochemical water splitting activity, *Ceram. Int.*, 2019, **45**, 6985–6993.

48 K. Govatsi, A. Seferlis, S. G. Neophytides and S. N. Yannopoulos, Influence of the morphology of ZnO nanowires on the photoelectrochemical water splitting efficiency, *Int. J. Hydrogen Energy*, 2018, **43**, 4866–4879.

49 J. Li, R. Miró, A. Wrzesińska-Lashkova, J. Yu, J. Arbiol, Y. Vaynzof, A. Shavel and V. Lesnyak, Aqueous Room-Temperature Synthesis of Transition Metal Dichalcogenide Nanoparticles: A Sustainable Route to Efficient Hydrogen Evolution, *Adv. Funct. Mater.*, 2024, **34**, 2404565, DOI: 10.1002/adfm.202404565.

50 X. Ding, F. Peng, J. Zhou, W. Gong, G. Slaven, K. P. Loh, C. T. Lim and D. T. Leong, Defect engineered bioactive transition metals dichalcogenides quantum dots, *Nat. Commun.*, 2019, **10**, 41, DOI: 10.1038/s41467-018-07835-1.

51 Y. Yang, R. Chen, J. Dai, D. Guo and L. Liu, Scale-up synthesis of RuCoNi hydroxide/sulfide heterostructures in alkali for the industrial current density, *Chem. Eng. J.*, 2023, **474**, 145971, DOI: 10.1016/j.cej.2023.145971.

52 L. Trotochaud, S. L. Young, J. K. Ranney and S. W. Boettcher, Nickel-Iron oxyhydroxide oxygen-evolution electrocatalysts: The role of intentional and incidental iron incorporation, *J. Am. Chem. Soc.*, 2014, **136**, 6744–6753, DOI: 10.1021/ja502379c.

53 T. Tang, S. Jiao, J. Han, Z. Wang and J. Guan, Partially crystallized Ni–Fe oxyhydroxides promotes oxygen evolution, *Int. J. Hydrogen Energy*, 2023, **48**, 5774–5782, DOI: 10.1016/j.ijhydene.2022.11.118.

54 M. Görlin, P. Chernev, P. Paciok, C.-W. Tai, J. de Araújo, T. Reier, M. Heggen, R. Dunin-Borkowski, P. Strasser and H. Dau, Formation of unexpectedly active Ni–Fe oxygen evolution electrocatalysts by physically mixing Ni and Fe oxyhydroxides, *Chem. Commun.*, 2019, **55**, 818–821, DOI: 10.1039/C8CC06410E.

55 J. C. Conesa, Electronic Structure of the (Undoped and Fe-Doped) NiOOH O2 Evolution Electrocatalyst, *J. Phys. Chem. C*, 2016, **120**, 18999–19010, DOI: 10.1021/acs.jpcc.6b06100.

56 C.-X. Zhao, B.-Q. Li, M. Zhao, J.-N. Liu, L.-D. Zhao, X. Chen and Q. Zhang, Precise anionic regulation of NiFe

9876 | *J. Mater. Chem. A*, 2025, **13**, 9865–9877

This journal is © The Royal Society of Chemistry 2025

hydroxysulfide assisted by electrochemical reactions for efficient electrocatalysis, *Energy Environ. Sci.*, 2020, **13**, 1711–1716, DOI: 10.1039/C9EE03573G.

57 B. Wang, C. Tang, H. Wang, B. Li, X. Cui and Q. Zhang, Anion-regulated hydroxysulfide monoliths as OER/ORR/HER electrocatalysts and their applications in self-powered electrochemical water splitting, *Small Methods*, 2018, **2**, 1800055.

58 R. Boppella, J. Tan, J. Yun, S. V Manorama and J. Moon, Anion-mediated transition metal electrocatalysts for efficient water electrolysis: Recent advances and future perspectives, *Coord. Chem. Rev.*, 2021, **427**, 213552.

59 M. Chauhan, K. P. Reddy, C. S. Gopinath and S. Deka, Copper cobalt sulfide nanosheets realizing a promising electrocatalytic oxygen evolution reaction, *ACS Catal.*, 2017, **7**, 5871–5879.

60 P. Thangasamy, S. Oh, S. Nam, H. Randriamahazaka and I. Oh, Ferrocene-incorporated cobalt sulfide nanoarchitecture for superior oxygen evolution reaction, *Small*, 2020, **16**, 2001665.

61 S.-W. Wu, S.-Q. Liu, X.-H. Tan, W.-Y. Zhang, K. Cadien and Z. Li, Ni3S2-embedded NiFe LDH porous nanosheets with abundant heterointerfaces for high-current water electrolysis, *Chem. Eng. J.*, 2022, **442**, 136105.

62 S. Wu, Y. Zhu, G. Yang, H. Zhou, R. Li, S. Chen, H. Li, L. Li, O. Fontaine and J. Deng, Take full advantage of hazardous electrochemical chlorine erosion to ultrafast produce superior NiFe oxygen evolution reaction electrode, *Chem. Eng. J.*, 2022, **446**, 136833.

63 P. J. Sharma, N. M. Solanki, K. H. Modi, U. Purohit, S. Siraj, P. Sahatiya, S. K. Gupta, P. N. Gajjar, C. K. Sumesh and P. M. Pataniya, Enhanced water and urea electrolysis at industrial scale current density using self-supported VxNi1-xO trifunctional catalysts, *Int. J. Hydrogen Energy*, 2024, **85**, 374–384, DOI: 10.1016/j.ijhydene.2024.08.352.

64 P. J. Sharma, N. A. Trivedi, K. S. Joseph, S. Siraj, P. Sahatiya, S. Dabhi, C. K. Sumesh and P. M. Pataniya, Self-supported V–Cu2S catalysts for green hydrogen production through alkaline water electrolysis, *Int. J. Hydrogen Energy*, 2024, **84**, 97–105, DOI: 10.1016/j.ijhydene.2024.08.224.

65 W. Liu, X. Wang, F. Wang, X. Liu, Y. Zhang, W. Li, Y. Guo, H. Yin and D. Wang, Electrochemical hydroxidation of sulfide for preparing sulfur-doped NiFe (oxy) hydroxide towards efficient oxygen evolution reaction, *Chem. Eng. J.*, 2023, **454**, 140030, DOI: 10.1016/j.cej.2022.140030.

This journal is © The Royal Society of Chemistry 2025

J. Mater. Chem. A, 2025, **13**, 9865–9877 | **9877**